

NUMERICAL SIMULATION OF INCOMPRESSIBLE TWO-PHASE FLOWS WITH A BOUSSINESQ-SCRIVEN INTERFACE STRESS TENSOR

ARNOLD REUSKEN AND YUANJUN ZHANG *

Abstract. We consider the numerical simulation of a three-dimensional two-phase incompressible flow with a *viscous* interface. The simulation is based on a *sharp interface* Navier-Stokes model and the *Boussinesq-Scriven* constitutive law for the interface viscous stress tensor. In the recent paper [Soft Matter 7, 7797–7804, 2011] a model problem with a spherical droplet in a Stokes Poiseuille flow with a Boussinesq-Scriven law for the surface viscosity has been analyzed. In that paper relations for the droplet migration velocity are derived. We relate the results obtained with our numerical solver for the two-phase Navier-Stokes model to these theoretical relations.

Key words. Two-phase flow, viscous interface, Boussinesq-Scriven

AMS subject classifications. 35Q30, 65M60

1. Introduction. Dynamic properties of interfaces, such as interfacial shear and dilatational viscosities and elasticity, can have a significant effect on the flow behavior. The effects caused by these properties can strongly influence the dynamics of emulsions, of biological fluids, of polymer blends and of many other soft matters. A better understanding of these phenomena is a major topic in the research field of *surface* rheology and in recent years a vast number of papers on dynamic properties of interfaces in soft matters has appeared. We refer to [21] for a recent overview. For the mathematical description of interfacial properties some classical models, like e.g. the Boussinesq-Scriven and the Kelvin Voigt models [24, 6] are known in the literature. These constitutive models were derived on a rather ad hoc basis and are applicable to only few, relatively simple, multiphase systems. In recent years there have been significant developments to systematically derive new (more general) constitutive laws for the stress-deformation behavior of interfaces using methods from nonequilibrium thermodynamics [16, 20]. The resulting models are far more advanced than the classical Boussinesq-Scriven and Kelvin Voigt models. Two-phase incompressible flows with an interfacial stress-deformation (i.e. a surface tension force) are usually modeled by either a diffusive interface or a sharp interface model. In this paper we restrict to the numerical simulation of the latter class of models. For numerical simulations based on a diffusive interface model we refer to the literature, e.g. [25, 26, 1]. In systems with incompressible fluids a sharp interface model typically consists of the Navier-Stokes equations for the bulk fluids with a surface tension force term on the right-hand side in the momentum equation, cf. section 2 for more details. This surface tension force is based on a certain interfacial stress-deformation constitutive law.

In this paper we do not treat modeling issues but address certain numerical simulation aspects for a class of two-phase incompressible flow sharp interface models with a *viscous* interface property. There are several reasons why in general two-phase flow problems have a very high numerical complexity. For example, the interface is unknown and due to this the flow problem is strongly nonlinear. Secondly, the surface tension force is localized at the (unknown) interface and often has a strong effect on the fluid dynamics. Thirdly, the pressure has a discontinuity across the interface,

*Institut für Geometrie und Praktische Mathematik, RWTH-Aachen University, D-52056 Aachen, Germany; email: reusken@igpm.rwth-aachen.de, zhang@igpm.rwth-aachen.de

and also the viscosity and density coefficients are discontinuous across the interface. Finally, the numerical simulation of such problems requires a suitable coupling of the fluid dynamics (e.g. Navier-Stokes solver) and the evolution of the interface (e.g. level set or VOF technique). There are several important issues relevant for the simulation of two-phase flows that are non-existent in *one*-phase incompressible flow problems. To handle these issues, special numerical techniques are required. Concerning the development and analysis of such special numerical methods only relatively few (compared to methods for one-phase flows) studies are available in the literature, cf. [11] for an overview.

Only recently there have appeared papers on the numerical simulation of *three-dimensional* two-phase flow problems with a *clean interface* model and either a constant surface tension coefficient or a variable surface tension coefficient (Marangoni effect). We are not aware of any literature in which numerical methods for handling a *viscous sharp interface* constitutive model are treated. In this paper we study this topic. We use the classical Boussinesq-Scriven constitutive law for describing the response of a viscous interface. The following two topics are addressed. Firstly, we present a method that is based on a variational formulation of the surface tension force and that can be used to discretize viscous interface forces. Secondly, we introduce a benchmark problem that is inspired by the recent paper [22]. In that paper analytical relations for the so-called migration velocity of a spherical droplet in a Stokes Poiseuille flow with Boussinesq-Scriven viscous interface forces are derived. The benchmark problem that we propose is a sharp interface Navier-Stokes model that in a certain sense is close to the stationary Stokes model studied in [22]. We present results of numerical experiments of our finite element solver applied to this benchmark problem.

The paper is organized as follows. In section 2 we present the mathematical model consisting of the Navier-Stokes equations combined with viscous interface forces based on the Boussinesq-Scriven constitutive law. We also explain the model for the stationary Stokes Poiseuille flow studied in [22]. In section 3 we describe the structure of our flow solver and briefly explain the main numerical methods used in it. A detailed explanation of the numerical treatment of the viscous interface force is given in section 3.5. In section 4 we introduce the benchmark problem and present results of simulations with our solver.

2. Mathematical models. In this section we introduce the models that we consider. In section 2.1 we recall a standard sharp interface model from the literature for describing the behavior of two-phase incompressible flows in which a Boussinesq-Scriven viscous interface stress tensor is used. Recently, a much simpler model with the same Boussinesq-Scriven tensor has been analyzed in [22]. This simpler model and results for that are given in section 2.2. In section 2.3 we discuss conditions under which the simple model is expected to be a reasonable approximation of the standard sharp interface model.

2.1. Two-phase Navier-Stokes equations with Boussinesq-Scriven interface stresses. Let $\Omega \subset \mathbb{R}^3$ be a domain containing two different immiscible incompressible phases. The time dependent subdomains containing the two phases are denoted by $\Omega_1(t)$ and $\Omega_2(t)$ with $\bar{\Omega} = \bar{\Omega}_1 \cup \bar{\Omega}_2$ and $\Omega_1 \cap \Omega_2 = \emptyset$. We assume that Ω_1 and Ω_2 are connected and $\partial\Omega_1 \cap \partial\Omega = \emptyset$ (i. e., Ω_1 is completely contained in Ω). The interface is denoted by $\Gamma(t) = \bar{\Omega}_1(t) \cap \bar{\Omega}_2(t)$. The bulk stress tensor is denoted by

$$\boldsymbol{\sigma} = -p\mathbf{I} + \mu\mathbf{D}(\mathbf{u}), \quad \mathbf{D}(\mathbf{u}) = \nabla\mathbf{u} + (\nabla\mathbf{u})^T,$$

with $p = p(x, t)$ the pressure, $\mathbf{u} = \mathbf{u}(x, t)$ the velocity and μ the bulk viscosity, which is assumed to be constant in each of the two bulk phases. We use the notation $[v]_\Gamma$ for the jump of v across Γ and introduce the projection operator $\mathbf{P} = \mathbf{I} - \mathbf{n}\mathbf{n}^T$, with $\mathbf{n} = \mathbf{n}_\Gamma$ the unit normal at the interface Γ (pointing from Ω_1 into Ω_2). The surface deformation tensor is given by $\mathbf{D}_\Gamma(\mathbf{u}) := \mathbf{P}(\nabla_\Gamma \mathbf{u} + (\nabla_\Gamma \mathbf{u})^T)\mathbf{P}$, with ∇_Γ the surface gradient. Based on the conservation laws for mass and momentum and using the linear Boussinesq-Scriven constitutive law [24] for describing an interface with a viscous response we obtain the following standard model, cf. for example [11],

$$\begin{cases} \rho_i \left(\frac{\partial \mathbf{u}}{\partial t} + (\mathbf{u} \cdot \nabla) \mathbf{u} \right) = -\nabla p + \rho_i \mathbf{g} + \operatorname{div}(\mu_i \mathbf{D}(\mathbf{u})) & \text{in } \Omega_i \times [0, T] \\ \operatorname{div} \mathbf{u} = 0 & \text{in } \Omega_i \times [0, T] \end{cases} \quad i = 1, 2, \quad (2.1)$$

$$[\mathbf{u}]_\Gamma = 0, \quad [\boldsymbol{\sigma} \mathbf{n}]_\Gamma = \operatorname{div}_\Gamma \boldsymbol{\sigma}_\Gamma, \quad (2.2)$$

$$\boldsymbol{\sigma}_\Gamma := [\tau + (\lambda_\Gamma - \mu_\Gamma) \operatorname{div}_\Gamma \mathbf{u}] \mathbf{P} + \mu_\Gamma \mathbf{D}_\Gamma(\mathbf{u}), \quad (2.3)$$

$$V_\Gamma = \mathbf{u} \cdot \mathbf{n} \quad \text{on } \Gamma. \quad (2.4)$$

The constants μ_i, ρ_i denote viscosity and density of the bulk phases in the subdomains Ω_i , $i = 1, 2$, and \mathbf{g} is an external volume force (gravity). The condition in (2.4), where V_Γ denotes the normal velocity of the interface, follows from immiscibility of the two phases. The first condition in (2.2) results from the viscosity of the phases. From momentum conservation one obtains the second relation in (2.2). The model for the surface stress tensor $\boldsymbol{\sigma}_\Gamma$ in (2.3) is the so-called Boussinesq-Scriven constitutive law, with a surface dilatational viscosity coefficient λ_Γ and a surface shear viscosity coefficient μ_Γ . We assume λ_Γ and μ_Γ to be constants with $\lambda_\Gamma \geq \mu_\Gamma \geq 0$. To make this problem well-posed we need suitable boundary conditions for \mathbf{u} , an initial condition $\mathbf{u}(x, 0)$ and an initial configuration of the interface $\Gamma(0)$. These will be specified at the end of this section.

The location of the interface $\Gamma(t)$ is unknown and is coupled to the fluid dynamics via the condition in (2.4) which determines the transport of the interface. Various approaches are used for approximating the interface. Most of these can be classified as either front-tracking or front-capturing techniques. In our solver we use a level set method [4, 15, 23] for capturing the interface.

The two Navier-Stokes equations in Ω_i , $i = 1, 2$, in (2.1) together with the interfacial conditions (2.2)-(2.4) can be reformulated in *one* Navier-Stokes equation on the whole domain Ω with a surface tension force term localized at the interface. Combining this with the level set method leads to the following model for the two-phase problem in $\Omega \times [0, T]$, with unknowns $\mathbf{u}(x, t)$, $p(x, t)$ and the level set function $\phi(x, t)$:

$$\begin{aligned} \rho(\phi) \left(\frac{\partial \mathbf{u}}{\partial t} + (\mathbf{u} \cdot \nabla) \mathbf{u} \right) &= -\nabla p + \rho(\phi) \mathbf{g} + \operatorname{div}(\mu(\phi) \mathbf{D}(\mathbf{u})) + \delta_\Gamma \operatorname{div}_\Gamma \boldsymbol{\sigma}_\Gamma \\ \operatorname{div} \mathbf{u} &= 0 \\ \frac{\partial \phi}{\partial t} + \mathbf{u} \cdot \nabla \phi &= 0. \end{aligned} \quad (2.5)$$

The level set function $\phi = \phi(x, t)$ characterizes the interface: $\phi < 0$ in Ω_1 , $\phi > 0$ in Ω_2 and $\phi = 0$ on Γ . The piecewise constant function $\rho(\phi)$ is given by $\rho(\phi) = \rho_1$ if $\phi < 0$ and $\rho(\phi) = \rho_2$ if $\phi > 0$. Similarly for $\mu(\phi)$. Appropriate initial and boundary conditions have to be added to make this problem well-posed. In the surface tension force term the Dirac functional δ_Γ is used. The numerical methods used in the remainder of this paper, in particular the finite element discretizations, are based

on a variational (weak) formulation of this model. We do not present this formulation here but restrict to the variational formulation of the surface tension force term, since the (numerical) treatment of this term is a main topic of this paper. The surface tension functional takes the form

$$f_\Gamma(\mathbf{v}) = \int_\Gamma (\operatorname{div}_\Gamma \boldsymbol{\sigma}_\Gamma) \cdot \mathbf{v} \, ds, \quad (2.6)$$

with \mathbf{v} from a suitable velocity test space. It is reasonable to restrict to test functions that are differentiable (in the usual Sobolev weak sense) and thus using a partial integration rule, this functional can be reformulated as

$$f_\Gamma(\mathbf{v}) = - \int_\Gamma \operatorname{tr}(\boldsymbol{\sigma}_\Gamma \nabla_\Gamma \mathbf{v}) \, ds = - \sum_{i=1}^3 \int_\Gamma (e_i^T \boldsymbol{\sigma}_\Gamma) \nabla_\Gamma v_i \, ds, \quad (2.7)$$

with e_i the i th basis vector in \mathbb{R}^3 and $\mathbf{v} = (v_1, v_2, v_3)^T$. This functional forms the basis for the numerical treatment of the Boussinesq-Scriven law as explained in section 3.5.

We now specify the domain, boundary and initial conditions that are used in the numerical experiments in section 4. For Ω we take a rectangular box with lengths L_x, L_y, L_z in the three coordinate directions. The interface $\Gamma(0)$ is defined as a sphere at the centreline of the box with radius r . The subdomain $\Omega_1(0)$ is the interior of this sphere. The boundary conditions for \mathbf{u} are as follows. On the z -boundaries ($z = \pm L_z$) we use periodic boundary conditions. On the y -boundaries we take Dirichlet no slip conditions ($\mathbf{u} = 0$). On the x -inflow boundary we prescribe a Poiseuille profile that is constant in z -direction and has the form

$$\mathbf{u}^P(y) = U_{center} \left(1 - \left(\frac{2y}{L_y}\right)^2\right) \vec{e}_x. \quad (2.8)$$

Here $U_{center} > 0$ denotes the speed of the flow on the centerline. On the x -outflow boundary we impose the zero stress condition $\boldsymbol{\sigma} \mathbf{n} = 0$. A sketch of the cross section of Ω at $z = 0$ is given in Fig. 2.1.

The values for the parameters $L_x, L_y, L_z, r, U_{center}$ will be specified further on.

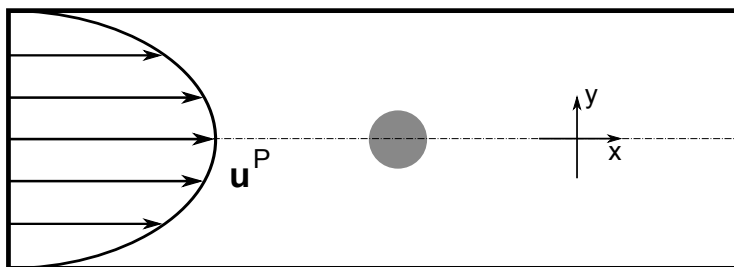


Fig. 2.1: Cross section of the domain used in numerical simulations

Finally we describe the initial condition $u(\cdot, 0) = u_0(\cdot)$ used in this paper. The function u_0 is taken as the solution of the *stationary Stokes* two-phase problem, obtained by putting the left-hand side in the momentum equation in (2.1) to zero and with interface conditions as in (2.2), (2.3). The boundary conditions and the interface $\Gamma(0)$ for this Stokes problem are the same as the ones specified above.

2.2. Model for a droplet in a stationary Stokes Poiseuille flow with Boussinesq-Scriven interface stresses. A, compared to the previous section, strongly simplified flow problem with Boussinesq-Scriven interface stresses is studied in the recent paper [22]. In that paper one considers an isolated spherical droplet in a Stokes Poiseuille flow with a jump in the hydrodynamic stress at the interface determined by surface viscous forces according to the Boussinesq-Scriven law. Besides viscous stresses also Marangoni effects, i.e., a variable τ is studied. Here, however, we restrict to the case without Marangoni effects (τ constant). Analytical relations for the so-called *migration velocity* are derived.

We give a more precise definition of the model used in [22]. The stationary bulk phase Ω_1 is a ball with radius r which has its centre on the x -axis, and $\Omega_2 = \mathbb{R}^3 \setminus \Omega_1$. In both phases creeping flow conditions are assumed, i.e.,

$$\begin{cases} -\mu_i \Delta \mathbf{u} + \nabla p = 0 & \text{in } \Omega_i \\ \operatorname{div} \mathbf{u} = 0 & \text{in } \Omega_i \end{cases} \quad i = 1, 2. \quad (2.9)$$

Instead of a boundary condition the far field condition

$$\mathbf{u}(\mathbf{x}) \rightarrow \mathbf{u}^P(\mathbf{x}) \quad \text{for } \|\mathbf{x}\| \rightarrow \infty, \quad (2.10)$$

with \mathbf{u}^P given by a Poiseuille flow profile

$$\mathbf{u}^P(y) = U_{center}(1 - \alpha y^2)\vec{\mathbf{e}}_x, \quad (2.11)$$

with a given constant $\alpha > 0$, cf. Fig. 2.1. At the interface Γ both kinematic and dynamic boundary conditions are imposed. Define the (droplet) mean velocity $\mathbf{U}_{\Omega_1} := \frac{1}{|\Omega_1|} \int_{\Omega_1} \mathbf{u} \, d\mathbf{x}$. The interface conditions are given by

$$[\mathbf{u}]_{\Gamma} = 0 \quad \text{on } \Gamma, \quad (2.12a)$$

$$\mathbf{u} \cdot \mathbf{n}_{\Gamma} = \mathbf{U}_{\Omega_1} \cdot \mathbf{n}_{\Gamma} \quad \text{on } \Gamma, \quad (2.12b)$$

$$[\mathbf{P}\boldsymbol{\sigma}\mathbf{n}]_{\Gamma} = \mathbf{P} \operatorname{div}_{\Gamma} \boldsymbol{\sigma}_{\Gamma} \quad \text{on } \Gamma. \quad (2.12c)$$

Note that (2.12b) enforces a normal velocity consistent with a rigid body translation. To obtain a well-posed problem only the *tangential* stress balance condition (2.12c) is imposed.

The model formulated above does not define a unique solution \mathbf{u} . If in (2.12b) the function $\mathbf{U}_{\Omega_1} \cdot \mathbf{n}_{\Gamma}$ is replaced by a *given* scalar function g on Γ then the model (2.9), (2.10), (2.12), with *data* g in the right-hand side in (2.12b) determines a unique solution, cf. [28]. Hence, for the above model to be well-posed we need an additional condition to determine the mean velocity vector \mathbf{U}_{Ω_1} . Note that $\int_{\Gamma} \operatorname{div}_{\Gamma} \boldsymbol{\sigma}_{\Gamma} \, ds = 0$. Hence the local force balance $[\boldsymbol{\sigma}\mathbf{n}]_{\Gamma} = \operatorname{div}_{\Gamma} \boldsymbol{\sigma}_{\Gamma}$ in (2.2) implies the global condition $\int_{\Gamma} [\boldsymbol{\sigma}\mathbf{n}]_{\Gamma} \, ds = 0$. This condition is not (necessarily) satisfied in the model above, since only tangential forces are considered in (2.12c). Hence, an additional condition that can be used to determine a unique solution is given by

$$\int_{\Gamma} [\boldsymbol{\sigma}\mathbf{n}]_{\Gamma} \, ds = 0, \quad (2.13)$$

which are three equations that can be used to determine the three unknowns in the average velocity vector \mathbf{U}_{Ω_1} .

The Poiseuille flow and spherical droplet are as shown in Fig. 2.1, if we delete the boundaries and extend the Poiseuille profile in y -direction and take it constant in x - and z -direction. Also note that there are no external forces (i.e., a neutrally buoyant droplet), but the interface stress tensor $\boldsymbol{\sigma}_\Gamma$ allows surface viscous forces (based on the Boussinesq-Scriven constitutive law).

The difference between the droplet mean velocity \mathbf{U}_{Ω_1} and the unperturbed Poiseuille flow on the x -axis $\mathbf{u}^P(0)$ is called the *migration velocity*:

$$\mathbf{U}_{mig} := \mathbf{U}_{\Omega_1} - \mathbf{u}^P(0). \quad (2.14)$$

In [22] explicit formulas for \mathbf{U}_{mig} are derived. The analysis relies on a representation of \mathbf{u} and \mathbf{u}^P in the basis of spherical harmonics. In the analysis it is essential that the droplet is *spherical*. The following result is from [22], with the dimensionless dilatational Boussinesq number $Bo^d := \frac{\lambda r}{\mu_2 r}$ and the viscosity ratio $\xi := \frac{\mu_1}{\mu_2}$:

$$\mathbf{U}_{mig} = -\frac{2Bo^d + 3\xi}{3(2 + 2Bo^d + 3\xi)} \alpha r^2 \mathbf{e}_x. \quad (2.15)$$

Note that there is a monotonic dependence of \mathbf{U}_{mig} on Bo^d and *no dependence* on the dimensionless shear Boussinesq number $Bo^s := \frac{\mu r}{\mu_2 r}$.

2.3. The stationary Stokes model as approximation for the general two-phase Navier-Stokes model. In the numerical experiments in section 4 we use the Navier-Stokes two-phase flow model given in section 2.1. Concerning the effect of viscous interface forces on the migration velocity we have the theoretical relation (2.15). The latter is derived for a stationary Stokes model on an unbounded domain and with interface conditions that differ from the ones used in the Navier-Stokes model. We expect, however, that this relation yields a good prediction of what happens in the Navier-Stokes model if the latter is “sufficiently close” to the model discussed in section 2.2. In this section we explain what is meant by “sufficiently close”.

We distinguish two steps. First we discuss the effect of considering the Stokes problem on a *bounded* domain instead of on \mathbb{R}^3 . After that, on the bounded domain, we discuss the validity of using Stokes as an approximation of the non-stationary Navier-Stokes equations.

The two-phase model is formulated in dimensional physical quantities. Therefore, below we add the units. We always use a fixed Poiseuille profile (2.11) with

$$U_{center} = 0.0125 \text{ m/s}, \quad \alpha = 5 \text{ 1/ms}. \quad (2.16)$$

From the unbounded to a bounded domain.

We consider the stationary Stokes model described above, but restrict to the clean interface case, i.e. with $\boldsymbol{\sigma}_\Gamma = \tau \mathbf{P}$. We scale such that $\mu_2 = 1 \text{ kg/ms}$. Instead of an unbounded domain we consider this model on a bounded rectangular box $\Omega = [0, L_x] \times [-\frac{1}{2}L_y, \frac{1}{2}L_y] \times [-\frac{1}{2}L_z, \frac{1}{2}L_z]$. We take the y -boundary such that the Poiseuille profile has zero values on these boundaries, as indicated in Fig. 2.1. Comparing (2.8) with (2.11) leads to $L_y = 0.1 \text{ m}$. In the stationary Stokes model we replace \mathbf{u} by $\mathbf{u} - \mathbf{U}_{\Omega_1}$, resulting in a homogeneous interface condition (2.12b). On the *bounded* domain Ω we consider the homogeneous Stokes equations as in (2.9). The interface

conditions are as in (2.12) with $\mathbf{U}_{\Omega_1} = 0$ and $\boldsymbol{\sigma}_\Gamma = \tau \mathbf{P}$. The boundary conditions are given by

$$\mathbf{u}(x, \pm \frac{1}{2}L_y, z) = -\mathbf{U}_{\Omega_1}, \quad (2.17a)$$

$$\mathbf{u}(0, y, z) = \mathbf{u}^P(y) - \mathbf{U}_{\Omega_1}, \quad (2.17b)$$

$$\boldsymbol{\sigma} \mathbf{n} = 0 \text{ at } x = L_x, \quad (2.17c)$$

$$\mathbf{u}(x, y, \pm \frac{1}{2}L_z) \cdot \mathbf{n} = 0. \quad (2.17d)$$

This model is implemented in the flow solver ngsflow [14].

REMARK 2.1. We briefly comment on a few aspects related to the implementation of the stationary Stokes model described above. The tetrahedral grids used are aligned to the interface Γ . The interface can be treated as an internal boundary. For the discretization $H(\text{div})$ conforming finite elements are used. The polynomial degree of the elements is varied in the experiments to check the accuracy of the discretization. The shape constraint $\mathbf{u} \cdot \mathbf{n} = 0$ is easy to implement as a Dirichlet condition on the internal boundary Γ . The tangential interfacial stress condition $[\mathbf{P}\boldsymbol{\sigma}\mathbf{n}]_\Gamma = 0$ is treated as a natural “internal boundary” condition. As indicated above, the model is not well-posed due to the fact that the boundary conditions in (2.17a), (2.17b) depend on the unknown average velocity vector \mathbf{U}_{Ω_1} . From symmetry arguments it is clear that \mathbf{U}_{Ω_1} has the direction $\vec{\mathbf{e}}_x$, i.e. $\mathbf{U}_{\Omega_1} = \beta \vec{\mathbf{e}}_x$ with an unknown scalar β . This scalar is determined by using the condition (2.13), but only in the x -direction, i.e. the scalar equation

$$g(\beta) := \vec{\mathbf{e}}_x \cdot \int_\Gamma [\boldsymbol{\sigma}\mathbf{n}]_\Gamma ds = 0. \quad (2.18)$$

For a given value the function $g(\beta)$ can be (numerically) evaluated as follows. The given β determines an average velocity $\mathbf{U}_{\Omega_1} = \beta \vec{\mathbf{e}}_x$. Using this the stationary Stokes model on the bounded domain Ω described above can be solved (sufficiently accurate). The resulting velocity field and pressure can be inserted in the stress tensor $\boldsymbol{\sigma}$ and thus the value of $g(\beta)$ can be determined. Using a simple root finding algorithm the zero of g , denoted by β^* , can be determined approximately. This results in the final migration velocity value $\mathbf{U}_{\Omega_1} = \beta^* \vec{\mathbf{e}}_x$.

Using this implementation we performed experiments for the case $\mu_1 = 2$, $\mu_2 = 1 \text{ kg/ms}$. Based on these experiments we choose $L_x = L_z = 0.3 \text{ m}$ and a droplet radius $r = 0.0125 \text{ m}$. For these values the numerically computed migration velocity differs (at most) approximately 1% from the theoretically predicted one in (2.15) (which corresponds to the unbounded domain case). In the remainder we keep these parameter values fixed, i.e., $L_y = 0.1 \text{ m}$, $L_x = L_z = 0.3 \text{ m}$ and $r = 0.0125 \text{ m}$ and U_{center} , α as in (2.16).

The theoretical migration velocity depends on the viscosity ratio ξ . We performed numerical simulations for the stationary Stokes model on the bounded domain Ω . The results of the experiments and the theoretically predicted correlation are shown in Figure 2.2.

We conclude that on this bounded domain and with boundary conditions as described in (2.17) we obtain a good agreement between theoretical predictions and numerical results.

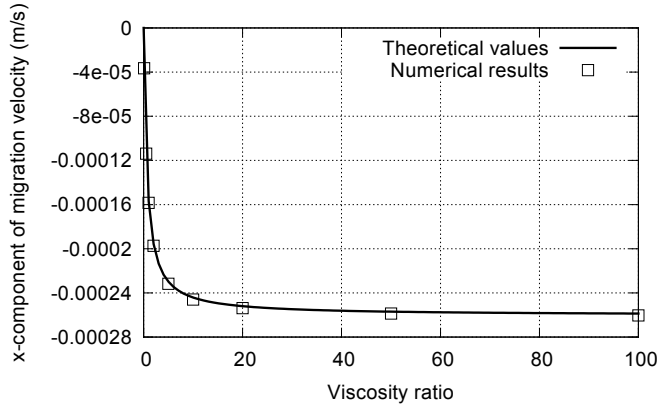


Fig. 2.2: Comparison of theoretical migration velocity and numerical results for various viscosity ratios ξ . Shown is the migration velocity component in flow direction \mathbf{e}_x .

The stationary Stokes model as approximation for the Navier-Stokes model.

In this section we relate the Navier-Stokes model described in section 2.1, cf. Fig. 2.1, to the stationary Stokes model on the bounded domain Ω with boundary conditions as in (2.17). From $U_{center} = 0.0125 \text{ m/s}$ and $r = 0.0125 \text{ m}$ we obtain a time scale: per second the droplet moves approximately over a distance comparable to its radius in flow direction. In the experiments we use a time interval $[0, T]$ with $T = 6 \text{ s}$.

In the Navier-Stokes model we have to specify ρ_i , μ_i and the surface tension coefficient τ . We restrict to systems in which the jumps in density and viscosity are “small”, e.g., both phases are liquids. For simplicity we set $\rho_1 = \rho_2$ (unit: kg/m^3) and as an example we take $\mu_1 = 2\mu_2$, i.e., $\xi = 2$. To characterize the fluid behavior the following dimensionless numbers are relevant:

$$Re = \frac{\rho_2 LU}{\mu_2}, \quad We = \frac{\rho_2 LU^2}{\tau}, \quad Ca = \frac{\mu_2 \hat{U}}{\tau}. \quad (2.19)$$

From the units introduced above, it follows that the surface tension coefficient τ has unit kg/s^2 . The Reynolds number relates the size of inertia to that of viscous stresses. The parameters L and U are typical length and velocity scales. In the setting here we can take $L = 0.1 \text{ m}$, $U = U_{center} = 0.0125 \text{ m/s}$. For the stationary Stokes model to be a reasonable approximation of the Navier-Stokes model it is necessary that $Re \ll 1$ holds. Hence we obtain the condition $\frac{\rho_2}{\mu_2} \ll 0.8 \cdot 10^3$. The Weber number relates the size of inertia to that of surface tension. For the Stokes model to be a reasonable approximation of the Navier-Stokes model it is necessary that $We \ll 1$ holds. This results in the condition $\frac{\rho_2}{\tau} \ll 0.64 \cdot 10^5$. The capillary number relates the size of the viscous stresses to that of the capillary stresses. For the Stokes model to be a reasonable approximation of the Navier-Stokes model, in the latter *the initial spherical droplet should keep its spherical shape*. This leads to the condition $Ca \ll 1$. For comparing the viscous and capillary stresses one can take a frame of reference with origin moving with speed U_{center} in direction \mathbf{e}_x . Hence, the size of the migration velocity is a better measure for the typical velocity size \hat{U} (close to the interface) than

the inflow velocity size U_{center} . The migration velocity is of the order of magnitude $\alpha r^2 = 5 \cdot 0.0125^2$, cf. (2.15). Hence, $Ca \ll 1$ leads to the condition $\frac{\mu_2}{\tau} \ll 1.3 \cdot 10^3$. We summarize the conditions obtained:

$$\frac{\rho_2}{\mu_2} \ll 0.8 \cdot 10^3, \quad \frac{\rho_2}{\tau} \ll 0.64 \cdot 10^5, \quad \frac{\mu_2}{\tau} \ll 1.3 \cdot 10^3. \quad (2.20)$$

In this parameter range we expect that the flow behavior, modeled by the incompressible two-phase Navier-Stokes equations, is such that the Stokes model yields a reasonable approximation. In particular the migration velocity behavior in the Navier-Stokes model should be similar to that for the Stokes flow (2.15) (in an unbounded domain). This will be investigated in section 4.

3. A Navier-Stokes two-phase flow solver. In this section we outline the numerical methods used in our solver for the two-phase flow model described in section 2.1, which is based on the DROPS package [5]. A detailed treatment of these methods is presented in [11]. Since in this paper we focus on the numerical treatment of the Boussinesq-Scriven law, the numerical treatment of the interface stress tensor is explained in more detail in section 3.5.

3.1. Spatial discretization and reconstruction of the interface. *Nested hierarchy of tetrahedral triangulations.* The spatial discretization is based on a hierarchy of tetrahedral grids. These grids are constructed in such a way that they are consistent (no hanging nodes) and that the hierarchy of triangulations is stable, [11]. An important property is that local refinement and coarsening are easy to realize.

Discretization of the level set equation. For discretization of the level set equation we use piecewise quadratic finite elements combined with the following streamline-diffusion stabilization. Let V_h be the space of continuous piecewise quadratics and $\phi_{0,h} \in V_h$ an approximation of the initial condition $\phi_0 = \phi(0)$. The spatial semi-discretization reads: Determine $\phi_h(t) \in V_h$, $t \in [0, T]$, with $\phi_h(0) = \phi_{0,h}$ and such that

$$\sum_{T \in \mathcal{T}_h} \left(\frac{\partial \phi_h}{\partial t} + \mathbf{u}_h \cdot \nabla \phi_h, v_h + \delta_T \mathbf{u}_h \cdot \nabla v_h \right)_{L^2(T)} = 0 \quad \text{for all } v_h \in V_h. \quad (3.1)$$

The vector field $\mathbf{u}_h \in \mathbf{V}_h$ is a finite element approximation of the velocity \mathbf{u} , cf. below, and $\phi_{0,h}$ is a finite element approximation of the initial condition $\phi(x, 0)$. The value of the stabilization parameter δ_T is based on the ansatz $\delta_T = ch_T \|\mathbf{u}_h\|_{L^\infty(T)}^{-1}$ (cf. [18]) and the constant c is chosen such that (for a class of model test problems) one has a good compromise between stability and consistency.

Reconstruction of the interface. For the discretization of the functional in (2.7) we determine an approximate reconstruction of the implicitly given zero level of the discrete level set function ϕ_h . The latter is a piecewise quadratic function on a tetrahedral triangulation \mathcal{T}_h . We introduce a regular refinement of \mathcal{T}_h , denoted by \mathcal{T}'_h , which is obtained by regularly subdividing each tetrahedron of \mathcal{T}_h into 8 child tetrahedra. Let $I(\phi_h)$ be the continuous piecewise *linear* function on \mathcal{T}'_h which interpolates ϕ_h at all vertices of all tetrahedra in \mathcal{T}'_h . The approximation of the interface Γ is defined by

$$\Gamma_h := \{ \mathbf{x} \in \Omega \mid I(\phi_h)(\mathbf{x}) = 0 \} \quad (3.2)$$

and consists of piecewise planar segments, which are either triangles or quadrilaterals. In [11] it is shown that under reasonable assumptions the approximation property

$\text{dist}(\Gamma, \Gamma_h) \leq ch^2$ holds.

Discretization of the Navier-Stokes equation. In finite element methods for *one*-phase flow problems the Taylor-Hood P_2 - P_1 pair is often used for discretization of velocity and pressure. In *two*-phase flow problems with surface tension forces the pressure is discontinuous across the interface and due to this the standard P_1 finite element space is not appropriate for discretization of the pressure variable. The so-called extended finite element method (XFEM) is much better suited for discretization of the pressure. We outline the main idea. More details and a comparison with the standard P_1 finite element method are given in [9, 17]. Let \mathcal{T}_h be a tetrahedral triangulation of Ω and

$$Q_h = \{q \in C(\Omega) \mid q|_T \in \mathcal{P}_1 \text{ for all } T \in \mathcal{T}_h\}$$

the standard finite element space of continuous piecewise linear functions. We define the index set $\mathcal{J} = \{1, \dots, n\}$, where $n = \dim Q_h$ is the number of degrees of freedom. Let $\mathcal{B} := \{q_j\}_{j=1}^n$ be the nodal basis of Q_h , i.e. $q_j(\mathbf{x}_i) = \delta_{i,j}$ for $i, j \in \mathcal{J}$ where $\mathbf{x}_i \in \mathbb{R}^3$ denotes the coordinate vector of the i -th degree of freedom. The idea of the XFEM method is to enrich the original finite element space Q_h by suitably chosen additional basis functions [13, 3]. In our case the finite element space Q_h is enriched by discontinuous basis functions q_j^Γ for $j \in \mathcal{J}_\Gamma := \{j \in \mathcal{J} \mid \text{meas}_2(\Gamma \cap \text{supp } q_j) > 0\}$, as discontinuities in the pressure only occur at the interface. Let $d : \Omega \rightarrow \mathbb{R}$ be the signed distance function, or an approximation to it, with d negative in Ω_1 and positive in Ω_2 . In our applications the discretization ϕ_h of the level set function ϕ is used for d . Using the Heaviside function H we define

$$H_\Gamma(x) := H(d(x)) = \begin{cases} 0 & x \in \Omega_1 \cup \Gamma, \\ 1 & x \in \Omega_2. \end{cases}$$

As we are interested in functions with a jump across the interface we define the so-called enrichment function $\Phi_j^H(x) := H_\Gamma(x) - H_\Gamma(\mathbf{x}_j)$ and a corresponding additional basis function $q_j^\Gamma := q_j \cdot \Phi_j^H$, $j \in \mathcal{J}'$. The second term in the definition of Φ_j^H is constant and may be omitted (as it does not introduce new functions in the function space), but ensures the nice property $q_j^\Gamma(\mathbf{x}_i) = 0$, i.e. q_j^Γ vanishes in all degrees of freedom. As a consequence, we have

$$\text{supp } q_j^\Gamma \subset \left(\text{supp } q_j \cap \bigcup_{T \in \mathcal{T}_h^\Gamma} T \right), \quad (3.3)$$

where $\mathcal{T}_h^\Gamma = \{T \in \mathcal{T}_h \mid \text{meas}_2(T \cap \Gamma) > 0\}$. Thus $q_j^\Gamma \equiv 0$ in all T with $T \notin \mathcal{T}_h^\Gamma$. The XFEM space that we use is given by

$$Q_h^\Gamma := \text{span}(\{q_j \mid j \in \mathcal{J}\} \cup \{q_j^\Gamma \mid j \in \mathcal{J}_\Gamma\}).$$

Note that this space depends on the location of the interface Γ . Approximation properties of this space are derived in [17]. In our solver, for the spatial discretization of the velocity and pressure we use the pair P_2 - Q_h^Γ , where P_2 is the standard finite element space of continuous piecewise quadratics and Q_h^Γ the XFEM space introduced above. In practice in the construction of the XFEM space instead of the interface Γ we use its numerical approximation Γ_h .

3.2. Time discretization and decoupling strategy. For the time discretization we apply an implicit one-step scheme to the coupled system (2.5). Since in general

the interface, and thus the pressure XFEM space, is changing as a function of time, it is natural to apply a Rothe approach (i.e., first time and then space discretization). We use a simple θ -scheme ($\theta = 1$: implicit Euler; $\theta = \frac{1}{2}$: Crank-Nicolson). Per time step an iterative method is applied to decouple the (discretized) Navier-Stokes equations from the (discretized) level set equation. The localized surface tension functional (2.7) in the Navier-Stokes momentum equation causes a strong stiffness in the coupled problem, cf. [2], and thus one has to be very careful in the decoupling strategy. A simple fixed point approach in which the available level set approximation is substituted into the Navier-Stokes equation, resulting in a new velocity field that is then substituted into the level set equation, etc., will in general result in a very severe time step restriction. A much better decoupling method (i.e., allowing a significantly larger time step) is obtained if one linearizes the surface tension based on the approximation $\Gamma(t_{n+1}) \approx \Gamma(t_n) + \Delta t \mathbf{u}(\cdot, t_n + 1)$. A detailed study of this linearization approach applied to the surface tension functional (2.7), (2.3), i.e., with the Boussinesq-Scriven constitutive law, will be presented in a forthcoming paper.

3.3. Re-initialization of the level set function. For numerical purposes it is advantageous to keep the level set function close to a signed distance function during the time evolution. To realize this a re-initialization (also called reparametrization) technique is needed. We apply a variant of the fast marching method (FMM) [12, 23]. This method can be applied to a quadratic finite element approximation of the level set function as follows. Let ϕ_h be a piecewise quadratic finite element function on the tetrahedral triangulation \mathcal{T}_h which has to be reparametrized. The function $I(\phi_h)$ is piecewise *linear* on the refined tetrahedral triangulation \mathcal{T}'_h of \mathcal{T}_h and Γ_h is the zero level of this function, cf. (3.2). As input for the FMM we need \mathcal{T}'_h , the zero level set Γ_h and $\text{sign}(I(\phi_h(v)))$ for all vertices v in \mathcal{T}'_h . Given this input, one can apply a FMM ([12, 23]), which results in a reparametrization that is piecewise *linear* on \mathcal{T}'_h . The values at the vertices in \mathcal{T}'_h of this function uniquely define a piecewise *quadratic* function on \mathcal{T}_h , which is defined to be the re-initialization of ϕ_h .

3.4. Iterative solvers. In each time step a discrete Navier-Stokes problem and a discrete level set equation must be solved. For the latter we use the GMRES method with a Gauss-Seidel preconditioner. The discrete Navier-Stokes equations are linearized using a relaxed defect correction algorithm given in [27]. This linearization results in Oseen problems of the form

$$\begin{pmatrix} \mathbf{A} & \mathbf{B}^T \\ \mathbf{B} & 0 \end{pmatrix} \begin{pmatrix} \mathbf{v} \\ \mathbf{q} \end{pmatrix} = \begin{pmatrix} \mathbf{r}_1 \\ \mathbf{r}_2 \end{pmatrix}.$$

For the iterative solution of these Oseen equations we apply the preconditioned generalized conjugate residual method (GCR), cf. [19]. This Krylov subspace method allows the use of a variable preconditioner. We use a block-preconditioner of the form

$$\mathbf{W} = \begin{pmatrix} \mathbf{Q}_A & 0 \\ \mathbf{B} & \mathbf{Q}_S \end{pmatrix},$$

where \mathbf{Q}_A is a preconditioner of the \mathbf{A} -block and \mathbf{Q}_S a preconditioner for the Schur complement $\mathbf{S} := \mathbf{B}\mathbf{A}^{-1}\mathbf{B}^T$. For \mathbf{Q}_A we use one standard multigrid V -cycle iteration for the discrete diffusion-convection-reaction equations in the \mathbf{A} -block. For \mathbf{Q}_S we use a scaled version of the BFB^T -preconditioner, which we now explain. In [8, 7] for discrete problems resulting from Hood-Taylor finite element discretization of

Navier-Stokes equations the following so-called $BF\mathbf{B}^T$ -preconditioner is introduced and analyzed:

$$\mathbf{Q}_S^{-1} = (\mathbf{B}\mathbf{M}_V^{-1}\mathbf{B}^T)^{-1}\mathbf{B}\mathbf{M}_V^{-1}\mathbf{A}\mathbf{M}_V^{-1}\mathbf{B}^T(\mathbf{B}\mathbf{M}_V^{-1}\mathbf{B}^T)^{-1},$$

where \mathbf{M}_V is the diagonal of the mass matrix in the velocity finite element space. In the application of this preconditioner two systems with the Poisson type matrix $\mathbf{B}\mathbf{M}_V^{-1}\mathbf{B}^T$ have to be solved (approximately). In our applications, instead of the standard Hood-Taylor pair we use the pair P_2 - Q_h^1 , i.e. we use the XFEM space for pressure discretization. It turns out that, due to basis functions with very small support, the conditioning of the matrix $\mathbf{B}\mathbf{M}_V^{-1}\mathbf{B}^T$ is often extremely bad. This, however, can be repaired by using a simple rescaling as follows. The matrix \mathbf{Q}_S^{-1} can also be represented as

$$\mathbf{Q}_S^{-1} = \mathbf{M}_Q^{-1/2}(\tilde{\mathbf{B}}\tilde{\mathbf{B}}^T)^{-1}\tilde{\mathbf{B}}\tilde{\mathbf{A}}\tilde{\mathbf{B}}^T(\tilde{\mathbf{B}}\tilde{\mathbf{B}}^T)^{-1}\mathbf{M}_Q^{-1/2}$$

with \mathbf{M}_Q the diagonal of the pressure mass matrix, $\tilde{\mathbf{B}} := \mathbf{M}_Q^{-1/2}\mathbf{B}\mathbf{M}_V^{-1/2}$ and $\tilde{\mathbf{A}} := \mathbf{M}_V^{-1/2}\mathbf{A}\mathbf{M}_V^{-1/2}$. The scaling (and thus the conditioning) of $\tilde{\mathbf{B}}\tilde{\mathbf{B}}^T$ is much better than that of $\mathbf{B}\mathbf{M}_V^{-1}\mathbf{B}^T$ and the performance of the preconditioner in this form is satisfactory.

3.5. Numerical treatment of Boussinesq-Scriven interface viscosity.

A main topic of this paper is the treatment of the Boussinesq-Scriven surface viscosity functional. In this section we introduce a new method for discretization of this functional. Inserting the Boussinesq-Scriven surface stress tensor in (2.7) and using $\mathbf{P}\nabla_\Gamma = \mathbf{P}\nabla$, we obtain the following weak form of the surface tension functional:

$$\begin{aligned} f_\Gamma(\mathbf{v}) &= -\tau \int_\Gamma \text{tr}(\mathbf{P}\nabla\mathbf{v}) \, ds \\ &\quad - (\lambda_\Gamma - \mu_\Gamma) \int_\Gamma \text{div}_\Gamma \mathbf{u} \, \text{tr}(\mathbf{P}\nabla\mathbf{v}) \, ds \\ &\quad - \mu_\Gamma \int_\Gamma \text{tr}(\mathbf{D}_\Gamma(\mathbf{u})\nabla\mathbf{v}) \, ds, \end{aligned} \tag{3.4}$$

with $\mathbf{P} = \mathbf{I} - \mathbf{n}\mathbf{n}^T$ and $\mathbf{D}_\Gamma(\mathbf{u}) = \mathbf{P}(\nabla\mathbf{u} + (\nabla\mathbf{u})^T)\mathbf{P}$. We assume a given piecewise planar approximation Γ_h of Γ as in (3.2). The piecewise constant unit normal vector to Γ_h is denoted by \mathbf{n}_h . Define $\mathbf{P}_h := \mathbf{I} - \mathbf{n}_h\mathbf{n}_h^T$. An obvious discretization is obtained if in (3.4) we replace \mathbf{u} by \mathbf{u}_h , Γ by Γ_h and \mathbf{P} by \mathbf{P}_h . In [10], however, it is shown that already for the case of a clean interface (τ constant, $\lambda_\Gamma = \mu_\Gamma = 0$) the approximation of \mathbf{P} by \mathbf{P}_h results in poor results. Another, significantly better, approximation of \mathbf{P} is readily available by using the *quadratic* finite element approximation ϕ_h . Define

$$\tilde{\mathbf{n}}_h(x) := \frac{\nabla\phi_h(x)}{\|\nabla\phi_h(x)\|}, \quad \tilde{\mathbf{P}}_h(x) := \mathbf{I} - \tilde{\mathbf{n}}_h(x)\tilde{\mathbf{n}}_h(x)^T, \quad x \in \Gamma_h, \, x \text{ not on an edge.}$$

In [9] it is shown that the use of $\tilde{\mathbf{P}}_h$ instead of \mathbf{P}_h as an approximation of \mathbf{P} leads to much better results. A heuristic explanation for this is that the projection $\tilde{\mathbf{P}}_h$ on the *unknown* zero level of the *known, piecewise quadratic*, discrete level set function ϕ_h contains more accurate geometric information (e.g. concerning curvature) than

the projection \mathbf{P}_h on the *known* zero level of the *piecewise linear*, interpolation of ϕ_h . Based on this, the first term on the right-hand side of (3.4) is approximated by

$$-\tau \int_{\Gamma_h} \text{tr}(\tilde{\mathbf{P}}_h \nabla \mathbf{v}) \, ds = -\tau \sum_{i=1}^3 \int_{\Gamma_h} (\tilde{\mathbf{P}}_h e_i)^T \nabla v_i \, ds. \quad (3.5)$$

The test function $\mathbf{v} = \mathbf{v}_h = (v_1, v_2, v_3)^T$ is from the finite element velocity space (piecewise quadratics). Using the identity

$$\text{div}_\Gamma \mathbf{u} = \text{div} \mathbf{u} - \mathbf{n}^T \nabla \mathbf{u} \mathbf{n},$$

the second term in (3.4) is approximated by

$$\begin{aligned} & -(\lambda_\Gamma - \mu_\Gamma) \int_{\Gamma_h} (\text{div} \mathbf{u}_h - \tilde{\mathbf{n}}_h^T \nabla \mathbf{u}_h \tilde{\mathbf{n}}_h) \text{tr}(\tilde{\mathbf{P}}_h \nabla \mathbf{v}) \, ds \\ & = -(\lambda_\Gamma - \mu_\Gamma) \sum_{i=1}^3 \int_{\Gamma_h} (\text{div} \mathbf{u}_h - \tilde{\mathbf{n}}_h^T \nabla \mathbf{u}_h \tilde{\mathbf{n}}_h) (\tilde{\mathbf{P}}_h e_i)^T \nabla v_i \, ds. \end{aligned} \quad (3.6)$$

The third term in (3.4) is discretized by

$$\begin{aligned} & -\mu_\Gamma \int_{\Gamma_h} \text{tr}(\tilde{\mathbf{P}}_h (\nabla \mathbf{u}_h + (\nabla \mathbf{u}_h)^T) \tilde{\mathbf{P}}_h \nabla \mathbf{v}) \, ds \\ & = -\mu_\Gamma \sum_{i=1}^3 \int_{\Gamma_h} (\tilde{\mathbf{P}}_h (\nabla \mathbf{u}_h + (\nabla \mathbf{u}_h)^T) \tilde{\mathbf{P}}_h e_i)^T \nabla v_i \, ds. \end{aligned} \quad (3.7)$$

The discretization of the Boussinesq-Scriven interface force functional is obtained by adding the three terms in (3.5), (3.6) and (3.7).

4. Benchmark problem and numerical experiments. In this section we present results of our numerical solver applied to the two-phase Navier-Stokes model described in section 2.1. Based on the analysis in section 2.3 we consider a specific benchmark problem that is “close to” the Stokes model studied in [22]. Hence, it makes sense to determine the droplet migration velocities numerically and compare the dependence of this scalar quantity on other parameters (ξ, Bo^s, Bo^d) to the dependencies derived in [22], e.g. (2.15). The results might be useful for validation of other codes that can handle Boussinesq-Scriven interface forces and therefore we summarize all parameters used. For the Poiseuille inflow profile we take (2.8) with $U_{center} = 0.0125 \, m/s$ and $L_y = 0.1 \, m$. The computational domain is given by $\Omega = [0, 0.3] \times [-0.05, 0.05] \times [-0.15, 0.15] \, m^3$. The boundary conditions on $\partial\Omega$ are given in section 2.1. The initial phase-1 domain $\Omega_1(0)$ is a sphere with radius $0.0125 \, m$ with center located at the centerline of Ω . The initial velocity $\mathbf{u}(0)$ is described in section 2.1. The time interval is $[0, 6] \, s$. In the experiments below we specify the choice of μ_i, ρ_i and $\tau, \lambda_\Gamma, \mu_\Gamma$. Based on the discussion in section 2.2, we should satisfy the conditions in (2.20). Clearly, a “very large” value for τ is advantageous from a theoretical point of view, in the sense that for a very large surface tension coefficient the moving droplet will remain (almost) spherical. On the other hand, very large τ values are numerically more difficult to handle since larger surface tension forces cause larger spurious velocities close to the interface. Hence, we have the dilemma that *a larger τ value reduces the modeling error but increases the numerical error.*

In our solver we use numerical methods as outlined in section 3. The surface force functional is implemented as described in section 3.5. In the numerical experiments we perform local refinement close to the interface. Illustrations of typical grids used and of a numerically computed inner circulation pattern are given in Figure 4.1.

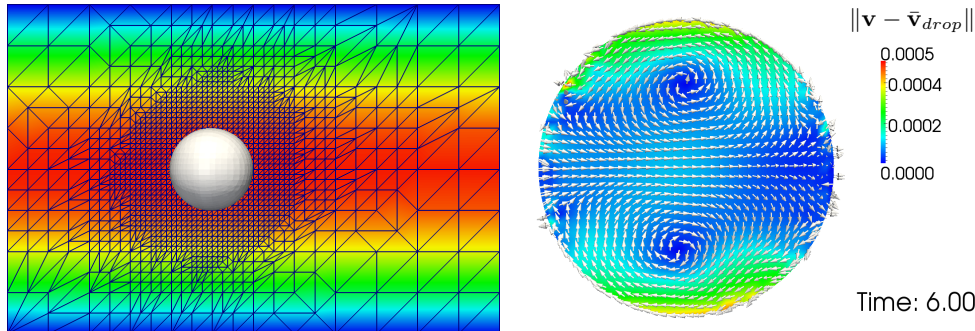


Fig. 4.1: Mesh with level 3 refinement (left) and numerically computed velocities field from non-stationary simulation at a cut plane. Shown is the computed velocity field minus droplet translation velocity.

In the experiments below we use the following local grid refinement. Within a distance of $0.0125 m$ from the interface the grid is locally refined. For the level 3 refinement the ratio between droplet diameter and tetrahedron diameter (for the tetrahedra in the refined region) is approximately 16. For the level 4 refinement this ratio is approximately 32. After each timestep, the grid is adaptively refined and coarsened according to the position of the interface. For the level three refinement the time step used is $0.005 s$.

As an illustration we show a result for a clean interface case (no viscous forces) with $\mu_1 = \mu_2 = \rho_1 = \rho_2 = 1$ and $\tau = 0.01, 0.1$ in Figure 4.2. In this experiment the droplet remains almost spherical for $\tau = 0.1$ and has a visible deformation for $\tau = 0.01$.

We now turn to experiments in which Boussinesq-Scriven surface tension forces are taken into account. In all the experiments we determine numerical migration velocities. This is done as follows. First, the x -component of the droplet mean velocity $U_{\Omega_1}(t) := \int_{|\Omega_1(t)|} \mathbf{u}(\mathbf{x}, t) \cdot \vec{\mathbf{e}}_x d\mathbf{x}$ is determined. A time dependent numerical migration velocity is given by $U_{mig}^{num}(t) := U_{\Omega_1}(t) - \mathbf{u}^P(0) \cdot \vec{\mathbf{e}}_x$. In turns out, cf. Fig. 4.3, that after a few time steps this scalar quantity is oscillating (due to numerical errors) around a mean value. This time averaged mean value, which we call the *numerical migration velocity*, is denoted by U_{mig}^{num} and can be compared to the scalar quantity $U_{mig}^{Stokes} := \mathbf{U}_{mig} \cdot \vec{\mathbf{e}}_x$ from (2.14). With respect to the accuracy of the numerical results it is important to note that the size of the derived quantity U_{mig}^{num} is significantly smaller than that of the computed velocities. The latter have a size comparable to $U_{center} = 0.0125 m/s$, whereas the numerical migration velocities have a size of approximately $0.00025 m/s$, i.e. are roughly a factor 50 smaller than the computed velocities.

Experiment 1. We take parameter values $\rho_1 = \rho_2 = 1$, $\mu_2 = 1$, $\xi = 2$, $\tau = 0.1$, $Bo^s = 0$. These values satisfy the conditions in (2.20). For different Bo^d values we determined the time dependent migration velocity $U_{mig}^{num}(t)$. Results are shown in

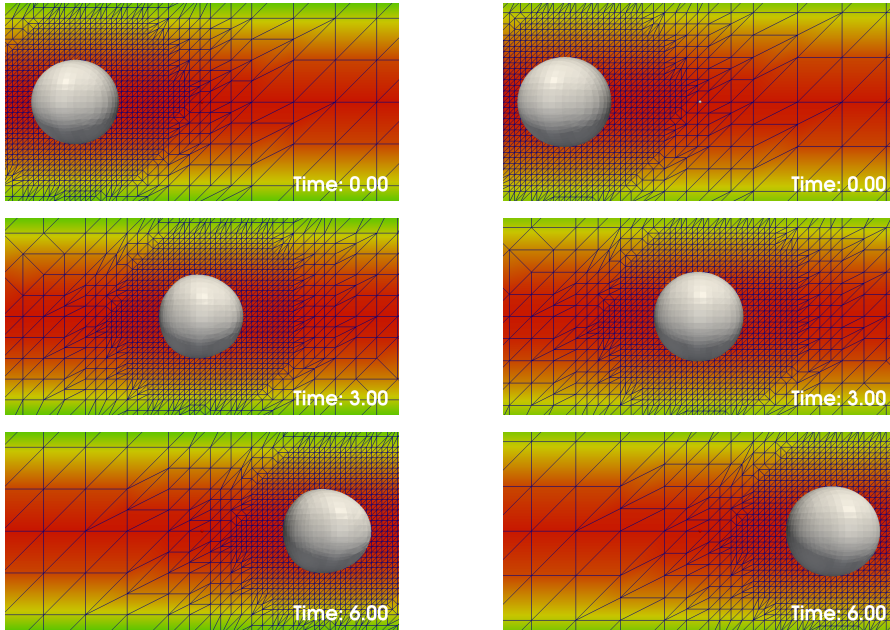


Fig. 4.2: Droplet shapes for $t = 0, 3, 6$ s (from top to bottom). Shown is the interface and the velocity field on a cut plane $z = 0$ m for surface tension coefficient $\tau = 0.01$ (left) and $\tau = 0.1$ (right).

Fig. 4.3. For a better view, in Fig. 4.3 the time dependent results are only shown for every 20 steps (every 0.1 s).

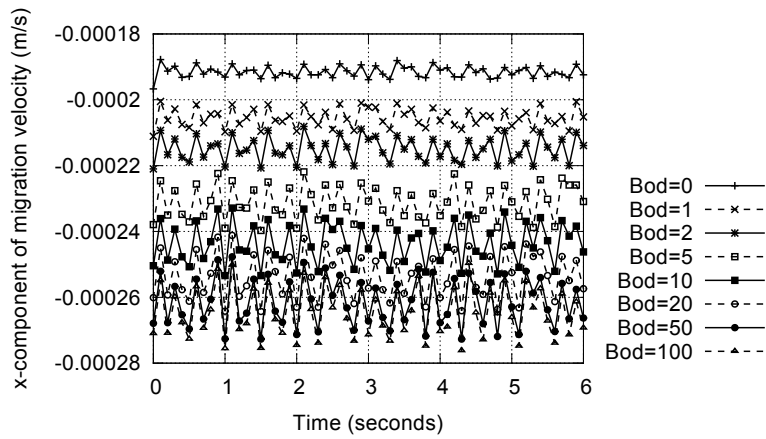


Fig. 4.3: Time dependent numerical migration velocity $U_{mig}^{num}(t)$ for $Bo^d = 0, 1, 2, 5, 10, 20, 50, 100$ at level 3 refinement.

We observe an oscillating behavior around a mean value. These oscillations are due to numerical errors and the amplitude of the oscillations increases if we take larger Bo^d values. This is due to the fact that for larger Bo^d numbers the viscous surface

forces increase and thus also the size of the numerical spurious velocities close to the interface. If we take the time average, we obtain the numerical migration velocity U_{mig}^{num} . These are indicated by \circ in Fig. 4.4. In the same figure we show the relation (2.14) for the theoretical Stokes migration velocity U_{mig}^{Stokes} with $\xi = 2$. Note that the numerical migration velocity for the Navier-Stokes model shows a similar dependence on Bo^d as the theoretical Stokes migration velocity. The difference between these two quantities is due to modeling errors (non-stationary Navier-Stokes instead of stationary Stokes) and numerical errors. Concerning the size of the numerical errors in U_{mig}^{num} we note that the results obtained on refinement level 3 are “close to grid convergence”. To illustrate this we consider the velocity profile on the line segment $y \in [-0.05, 0.05]$ in the cut plane $z = 0$ which passes the center of the droplet at $t = 2$. In Fig. 4.5 the x -component of this velocity calculated on the levels 2, 3, 4 for $Bo^d = 1$ are shown together with the background Poiseuille profile. The result on the level 2 refinement shows significant differences from the level 4 result, whereas the level 3 result can hardly be distinguished from the level 4 result. For larger Bo^d values the numerical errors increase, due to the larger surface tension forces. To illustrate this, for $Bo^d = 10$ and the time interval $[0, 2]$ s we determined the numerical migration velocity U_{mig}^{num} on the refinement levels 2,3,4. The values are respectively $U_{mig}^{num} = -2.584, -2.474, -2.390$ in unit $10^{-4} m/s$. The theoretical Stokes migration velocity for this case has value $-2.418 \cdot 10^{-4} m/s$.

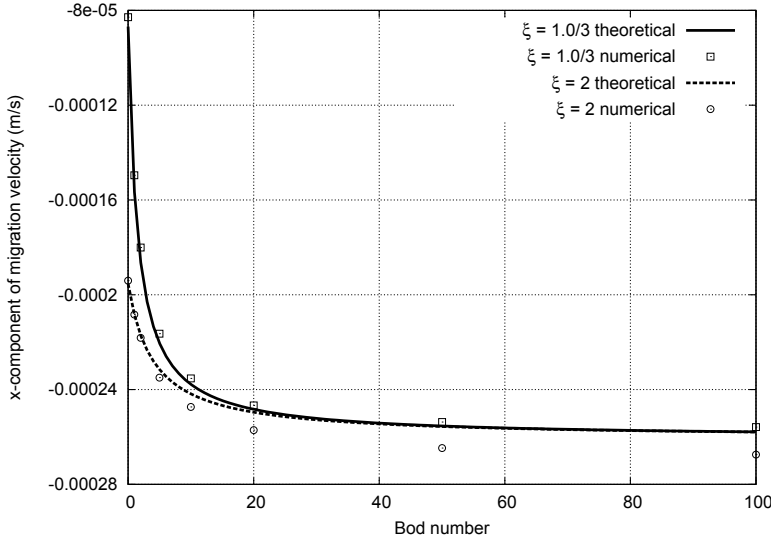


Fig. 4.4: Numerical migration velocity U_{mig}^{num} for $Bo^d = 0, 1, 2, 5, 10, 20, 50, 100$ at level 3 refinement. The cases $\xi = 2$ and $\xi = \frac{1}{3}$ are shown.

Experiment 2. We take $\xi = \frac{1}{3}$. For this case the theoretical relation for the Stokes migration velocity differs significantly from the case $\xi = 2$ (considered in Experiment 1), in particular for small Bo^d values. The two curves for $\xi = 2$ and $\xi = \frac{1}{3}$ are shown in Fig. 4.4. For the Navier-Stokes model the other parameters are taken the same as in Experiment 1, i.e., $\rho_1 = \rho_2 = 1, \mu_2 = 1, \tau = 0.1, Bo^s = 0$. For different Bo^d values

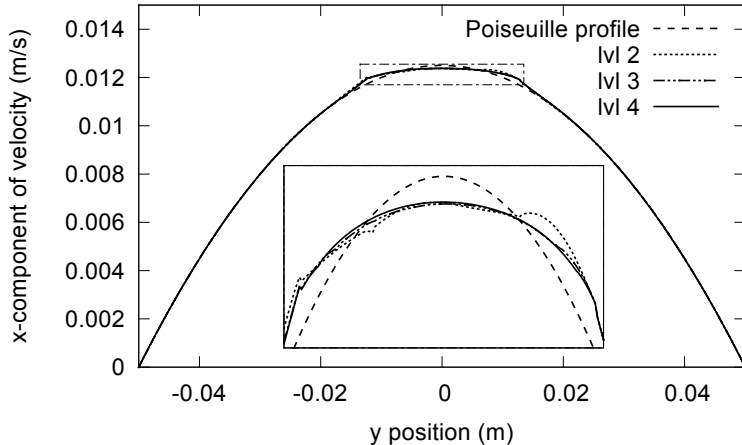


Fig. 4.5: Numerical velocity (x -component) for $Bo^d = 1$ at level 2, 3, 4 refinements. Shown are velocity profiles at time $t = 2$ s.

we determined, on refinement level 3, the numerical migration velocity U_{mig}^{num} . The results are indicated by \square in Fig. 4.4. Note that these are very close to the theoretical Stokes migration velocities. As indicated in Experiment 1, for larger Bo^d values the numerical values on the level 3 refinement are not (fully) converged, i.e., on finer grids and with smaller time steps these values might vary slightly. The dependency of this numerical migration velocity U_{mig}^{num} on Bo^d is then still very similar to that of the theoretical Stokes migration velocity.

Experiment 3. The densities ρ_1 and ρ_2 do not influence the theoretical Stokes migration velocity. As long as the conditions in (2.20) are satisfied, we expect the migration velocity obtained from the Navier-Stokes model to be close to that of the Stokes model. Therefore, if we keep all parameters fixed but only increase the ρ_i values, we expect that if the conditions in (2.20) are still satisfied then the numerical migration velocity should be essentially independent of the ρ_i values. In this experiment we verify this claim. We take $\rho_1 = \rho_2 = 100$ and all other parameters the same as in Experiment 1, i.e., $\mu_2 = 1$, $\xi = 2$, $\tau = 0.1$, $Bo^s = 0$. Results for the numerical migration velocity, computed on the level 3 refinement, are given in the fourth column in Table 4.1. Indeed, the results are (almost) the same as the one from Experiment 1 (with $\rho_1 = \rho_2 = 1$).

Experiment 4. The theoretical Stokes migration velocity U_{mig}^{Stokes} does *not* depend on the shear Boussinesq number, cf. (2.14). Hence, as long as the conditions in (2.20) are satisfied, we expect this to hold for the numerical migration velocity, too. In this experiment we verify this claim. We take the same parameter values as in Experiment 1, but now with varying Bo^s instead of $Bo^s = 0$. We take $Bo^s = Bo^d$, or, equivalently, $\lambda_\Gamma = \mu_\Gamma$. In Experiment 1 we used $Bo^s = 0$ and $Bo^d \neq 0$. In that case, in the Navier-Stokes model the shear interface viscosity term (3.7) equals zero and only the dilatational term (3.6) causes viscous interface effects. If we now take $Bo^s = Bo^d$, then the opposite happens: the dilatational interface viscosity term (3.6) equals zero and only the shear term (3.6) causes viscous interface effects. Hence, in Experiment

Bo^d	Stokes model	Exp. 1	Exp. 3	Exp. 4
0	-1.953	-1.940	-1.940	-
1	-2.083	-2.084	-2.084	-2.084
5	-2.315	-2.350	-2.350	-2.349
10	-2.418	-2.473	-2.473	-2.477
50	-2.556	-2.647	-2.647	-2.651
100	-2.579	-2.675	-2.674	-2.689

Table 4.1: Numerical migration velocity U_{mig}^{num} in different experiments (unit $10^{-4} m/s$). Simulation on level 3 refinement.

1 ($Bo^s = 0$) and in this experiment ($Bo^s = Bo^d$) different terms, (3.6) and (3.7), are used in the simulation of the Navier-Stokes model. Nevertheless we expect similar numerical migration velocities. The results for the case $Bo^s = Bo^d$ are presented in the last column in Table 4.1. Indeed these values are (almost) the same as the one from Experiment 1.

Acknowledgement. The authors acknowledge funding by the German Science Foundation (DFG) through the Cluster of Excellence “Taylor-Made Fuels from Biomass” at the RWTH Aachen University.

REFERENCES

- [1] S. Aland, J. Lowengrub, and A. Voigt. A continuum model of colloid stabilized interfaces. *Physics of Fluids*, 23:062103, 2011.
- [2] E. Bänsch. Finite element discretization of the Navier-Stokes equations with a free capillary surface. *Numer. Math.*, 88:203–235, 2001.
- [3] T. Belytschko, N. Mos, S. Usui, and C. Parimi. Arbitrary discontinuities in finite elements. *International Journal for Numerical Methods in Engineering*, 50(4):993–1013, 2001.
- [4] Y.C. Chang, T.Y. Hou, B. Merriman, and S. Osher. A level set formulation of eulerian interface capturing methods for incompressible fluid flows. *Journal of Computational Physics*, 124(2):449 – 464, 1996.
- [5] DROPS package for simulation of two-phase flows.
<http://www.igpm.rwth-aachen.de/DROPS/>.
- [6] D.A. Edwards, H. Brenner, and D.T. Wasan. *Interfacial Transport Phenomena and Rheology*. Butterworth-Heinemann, Boston, 1991.
- [7] H. Elman, V.E. Howle, J. Shadid, R. Shuttleworth, and R. Tuminaro. Block preconditioners based on approximate commutators. *SIAM J. on Scientific Computing*, 27(5):1651–1668, 2006.
- [8] H. Elman, D. Silvester, and A. Wathen. *Finite Elements and Fast Iterative Solvers*. Oxford University Press, Oxford, 2005.
- [9] S. Groß and A. Reusken. An extended pressure finite element space for two-phase incompressible flows with surface tension. *J. Comp. Phys.*, 224:40–58, 2007.
- [10] S. Groß and A. Reusken. Finite element discretization error analysis of a surface tension force in two-phase incompressible flows. *SIAM J. Numer. Anal.*, 45(4):1679–1700, 2007.
- [11] S. Gross and A. Reusken. *Numerical Methods for Two-phase Incompressible Flows*, volume 40 of *Springer series in computational mathematics*. Springer, Heidelberg, 2011.
- [12] R. Kimmel and J. A. Sethian. Computing geodesic paths on manifolds. *Proceedings of the National Academy of Sciences*, 95(15):8431–8435, 1998.
- [13] N. Mos, J. Dolbow, and T. Belytschko. A finite element method for crack growth without remeshing. *International Journal for Numerical Methods in Engineering*, 46(1):131–150, 1999.
- [14] ngsflow flow solver package with different applications in 3D and 2D for Netgen/NGSolve.

- <http://sourceforge.net/projects/ngsflow/>.
- [15] S. Osher and R.P. Fedkiw. Level set methods: An overview and some recent results. *Journal of Computational Physics*, 169(2):463 – 502, 2001.
 - [16] H.C. Öttinger, D. Bedeaux, and D.C. Venerus. Nonequilibrium thermodynamics of transport through moving interfaces with application to bubble growth and collapse. *Phys. Rev. E*, 80:021606, 2009.
 - [17] A. Reusken. Analysis of an extended pressure finite element space for two-phase incompressible flows. *Comput. Vis. Sci.*, 11:293–305, 2008.
 - [18] H.-G. Roos, M. Stynes, and L. Tobiska. *Numerical Methods for Singularly Perturbed Differential Equations — Convection-Diffusion and Flow Problems*, volume 24 of *Springer Series in Computational Mathematics*. Springer-Verlag, Berlin, 1996.
 - [19] Y. Saad. *Iterative methods for sparse linear systems*. Society for Industrial and Applied Mathematics, Philadelphia, PA, second edition, 2003.
 - [20] L.M.C. Sagis. Dynamics of encapsulation and controlled release systems based on water-in-water emulsions: Liposomes and polymersomes. *Physica A*, 388:2579–2587, 2009.
 - [21] L.M.C. Sagis. Dynamic properties of interfaces in soft matter: experiments and theory. *Rev. Mod. Phys.*, 83(4):1367, 2011.
 - [22] J. T. Schwalbe, F. R. Phelan, Jr., P. M. Vlahovska, and S. D. Hudson. Interfacial effects on droplet dynamics in poiseuille flow. *Soft Matter*, 7:7797–7804, 2011.
 - [23] J. A. Sethian. *Level set methods and fast marching methods*. Cambridge University Press, 1999.
 - [24] J Slattery, Leonard Sagis, and E.-S. Oh. *Interfacial Transport Phenomena*. Springer, New York, second edition, 2007.
 - [25] K. Teigen, X. Li, J. Lowengrub, F. Wang, and A. Voigt. A diffusion-interface approach for modelling transport, diffusion and adsorption/desorption of material quantities on a deformable interface. *Comm. Math. Sci.*, 7:1009–1037, 2009.
 - [26] K. Teigen, P. Song, J. Lowengrub, and A Voigt. A diffusive-interface method for two-phase flows with soluble surfactants. *J. Comp. Phys.*, 230:375–393, 2010.
 - [27] S. Turek. *Efficient solvers for incompressible flow problems: An algorithmic approach in view of computational aspects*, volume 6 of *LNCSE*. Springer, Berlin, Heidelberg, 1999.
 - [28] R. Verfürth. Finite element approximation of incompressible Navier-Stokes equations with slip boundary condition. *Numer. Math.*, 50:697–721, 1987.